ACS OMEGA

Article

Cite This: ACS Omega 2019, 4, 12938−12947

http://pubs.acs.org/journal/acsodf

Flow-Through Optical Chromatography in Combination with Confocal Raman Microspectroscopy: A Novel Label-Free Approach To Detect Responses of Live Macrophages to Environmental Stimuli

Qin Lu,* Daniel E. Barlow, Dhanya Haridas, Braden C. Giordano, Harold D. Ladouceur, Joel D. Gaston,† Greg E. Collins, and Alex V. Terray‡

Chemistry Division, Naval Research Laboratory, 4555 Overlook Avenue SW, Washington, D.C. 20375, United States

ABSTRACT: Flow-through optical chromatography (FT-OC), an advanced mode of optical chromatography, achieved baseline separation of a mixture of silica microparticles (SiO_2, 1.00 and 2.50 μm) and a mixture of polystyrene microparticles (PS, 1.00, 2.00, and 3.00 μm) based on particle size. Comparisons made between experimentally determined velocities for the microparticles and theoretically derived velocities from Mie theory and Stokes' law validated the data collection setup and the data analysis for FT-OC. A population shift in live macrophages (cell line IC-21, ATCC TIB-186) responding to environmental stimuli was sensitively detected by FT-OC. The average velocity of macrophages stressed by nutritional deprivation was decreased considerably together with a small but statistically significant increase in cell size. Mie scattering calculations demonstrated that the small increase in cell size of macrophages stressed by nutritional deprivation was not entirely responsible for this decrease. Confocal fluorescence microscopy and atomic force microscopy (AFM) studies revealed morphological changes of macrophages induced by nutritional deprivation, and these changes were more likely responsible for the decrease in average velocity detected by FT-OC. Confocal Raman microspectroscopy was used to shed light upon biochemical transformations of macrophages suffering from nutritional deprivation.

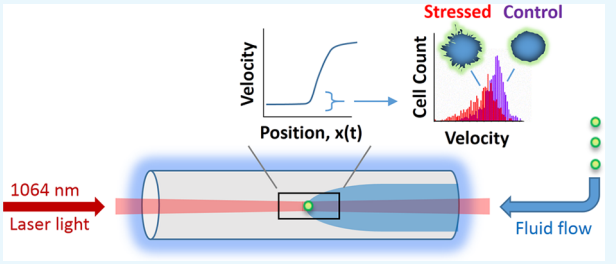

INTRODUCTION

Innate immune cells such as neutrophils, macrophages, and natural killer cells play key roles in the early defense against invading pathogens. Detecting stimuli at the single-cell level and initiating cascading response mechanisms, they are essentially living sensors to the onset of infection or exposure events. Analytical methods sensitive to physiological changes of individual immune cells could thus allow early exposure detection before symptoms appear, providing valuable increased time windows for countermeasures. Microfluidic flow-cytometry-based methods are appealing with capabilities for high-throughput analysis of bio-physical/chemical properties with sensitivity at the single-cell level.[1] However, rather than running a multitude of high-specificity, label-dependent assays for unknown targets, label-free methods with broad specificity and minimal sample preparation requirements are attractive where detection of initial physiological shifts could then prompt further, more targeted diagnosis.

Label-free flow cytometry approaches that are widely available with sensitivity to cellular biophysical properties include forward/side light-scatter detection, providing sensitivity to the refractive index, size, and granularity of cells.[1] Other cellular biophysical properties that can be probed by microfluidic-based methods include impedance[2] and cellular deformability.[3] High-throughput imaging cytometry supported by computational analysis is also being utilized.[4] The rationale in sensing biophysical changes is that they can accompany the complex biochemistry of immune cell activation and may be correlated to varying degrees. Raman spectroscopy is an example of another label-free method that has been demonstrated with microfluidic analysis[5,6] and can directly probe biochemical changes.

Optical chromatography (OC), originally termed by Kaneta et al.,[7] is an additional microfluidic-based, label-free technique capable of separating particles[8] and carrying out dynamic analysis of single live cells.[9] OC shares some similarities with optical tweezers.[10,11] Both use a laser and involve the interplay of two forces exerted on the particle of interest. Optical tweezers use a highly focused laser beam, and the two forces involved in the manipulation of particles are the scattering force (or radiation pressure force), which propels particles along the direction of light propagation, and the gradient force, which attracts the particle along the spatial gradient of light intensity to the focal point of the focused beam. OC uses a weakly focused laser beam on particles in a microfluidic flow, and particle discrimination relies upon the interaction of the radiation pressure force against the viscous drag force. The selectivity of OC is dependent on the intrinsic physical/biophysical nature of the particle/cell such as the size, shape, refractive index, surface roughness, and cellular structure.

Received: May 23, 2019
Accepted: July 12, 2019
Published: July 31, 2019

DOI: 10.1021/acsomega.9b01162
ACS Omega 2019, 4, 12938−12947

Table 1. Radiation Pressure Force Calculation Using Mie Theory and Average Velocities Comparison between Experimental Data and Calculated Values

particle	size (μm)	g	$C_{pr} \times 10^{13}$ (m^2)	F_{pr} (pN)	$V_{(laser\text{-}off)} \times 10^4$ (m/s)	$V_{exp} \times 10^4$ (m/s)	$V_{cal} \times 10^4$ (m/s)
SiO_2	1.00 ± 0.10	0.87	0.25	0.55	8.9 ± 0.43	8.77 ± 0.16	8.35
	2.50 ± 0.25	0.96	2.61	5.66	8.9 ± 0.43	6.74 ± 0.32	6.53
PS	1.00 ± 0.03	0.86	1.11	2.41	17.5 ± 0.57	11.8 ± 0.19	14.9
	2.00 ± 0.10	0.93	6.48	14.10	17.5 ± 0.57	6.79 ± 0.13	10.00
	3.00 ± 0.15	0.93	17.30	37.60	17.5 ± 0.57	3.42 ± 0.14	4.21
macrophage	10.0 ± 1.1	0.99	14.20	30.50	11.8 ± 0.49	6.37 ± 0.36	8.76
	10.2 ± 1.3	0.99	14.70	31.91	11.8 ± 0.49	5.90 ± 0.48	8.48

To date, OC has received limited attention, but for the application outlined here, it is a potentially valuable approach. One of the advantages of OC is its flexibility of operating either in the static mode for precise single-cell analysis or flow-through mode FT-OC with high throughput. In a static OC mode, laser power is fixed, and the flow rate of the fluid is adjusted in order to balance a single particle/cell at a predetermined position within the flow channel. Any intrinsic differences between particles/cells can be detected from changes in the flow rate, which correlates to changes in radiation pressure forces experienced by the particles/cells. Size differences as small as 70 nm between polymer microspheres, refractive index differences well below 0.06, and high refractive index coatings as small as 14 nm have been detected.[12,13] Additional information about the particles/cells can also be derived from optical images and light scattering patterns by the particles/cells. Raman scattered light can also be analyzed offering additional potential for integrated data acquisition.

FT-OC is an advanced mode of OC that also relies on the interplay of the radiation pressure force and the viscous drag force. Instead of balancing a single particle/cell at a predetermined position, FT-OC uses a properly chosen fluid flow rate against a fixed laser power and allows the particles/cells carried by the fluid to pass through the detection window continuously. The information collected by FT-OC includes the average velocity, average cross-sectional area, shape, and morphology of the individual particle/cell. Due to the nature of uninterrupted measurement of particles/cells passing through the detection window, FT-OC has a much higher throughput than static OC and scans hundreds of cells per minute. Thus, FT-OC offers configurational flexibility and compatibility for integrated acquisition of complimentary data for multivariate analysis. Here, we report the first demonstration of FT-OC in the rapid baseline separation of microparticles based on their size differences as well as the sensitive label-free detection of live macrophages undergoing autophagy in response to environmental stimuli, in this case, nutritional deprivation. Macrophages, although tissue resident cells, are highly amenable to laboratory culturing and thus serve as useful models for method development. Autophagy is a cellular process in which cytoplasmic contents are degraded within the lysosome/vacuole, and the resulting macromolecular constituents are recycled.[14] The macrophage innate immune response and autophagic processes are closely connected and modulated by TLR (Toll-like receptor) activation, inflammasome activation, and bacterial infection.[15]

In our previous work on label-free detection of *Bacillus anthracis* spore uptake in macrophages using static OC,[16] an increased radiation pressure force was observed on macrophages that phagocytosed *Bacillus anthracis* spores when compared to control cells. In the present study, biophysical changes of IC-21 macrophages induced by autophagy were sensitively detected by FT-OC as manifested by the increased radiation pressure force experienced by cells undergoing autophagy. Atomic force microscopy (AFM), confocal microscopy, and confocal Raman microscopy analyses are also used for additional correlation of bio-physcial/chemical changes with the observed population shifts from FT-OC.

RESULTS AND DISCUSSION

Basic Theory of Radiation Pressure Force. When an electromagnetic wave interacts with a small particle, the wave radiation can be scattered or absorbed by the particle. These interactions result in a momentum transfer from the radiation to the particle. This momentum transfer creates a force on the particle, which is referred to as the radiation pressure force. For a plane electromagnetic wave of incident intensity I_0, the radiation pressure force, F_{pr}, depends upon the radiation pressure cross section C_{pr} and the phase velocity of the light in the surrounding medium of refractive index n_1. The equation for the radiation pressure force is given by Kerker[17]

$$F_{pr} = I_0 \frac{C_{pr}}{c} n_1 \tag{1}$$

where c denotes the speed of light in vacuum. If the incident radiation is from a laser beam with a Gaussian profile, the intensity distribution is given by[18]

$$I_0 = \frac{2P}{A_{beam}} \tag{2}$$

where P denotes the laser power and A_{beam} is the beam area. The equation for the radiation pressure force from a Gaussian beam is given by

$$F_{pr} = \frac{2Pn_1}{c}\left(\frac{a}{w_0}\right)^2 C_{pr} \tag{3}$$

In this equation, a is the radius of the spherical particle, and w_0 is the beam waist or radius. The radiation pressure cross section C_{pr} for a spherical particle of radius a can be calculated from Mie theory.

In Mie theory, one defines dimensionless radiation pressure efficiency factor Q_{pr} as

$$Q_{pr} = \frac{C_{pr}}{G} \tag{4}$$

where $G = \pi a^2$ is the spherical particle's geometrical cross section. The radiation pressure efficiency factor is given by

$$Q_{pr} = Q_{ext} - Q_{sca}\langle \cos\theta \rangle \tag{5}$$

DOI: 10.1021/acsomega.9b01162
ACS Omega 2019, 4, 12938−12947

where Q_{ext} is the extinction efficiency factor, Q_{sca} is the scattering efficiency factor, and $\langle \cos \theta \rangle$ is the asymmetry factor g. If the particle's refractive index is a real number, there is no absorption, and

$$Q_{ext} = Q_{sca} \tag{6}$$

Thus, for a nonabsorbing particle, the expression for the radiation pressure efficiency factor reduces to

$$Q_{pr} = Q_{ext}(1 - \langle \cos \theta \rangle) = Q_{ext}(1 - g) \tag{7}$$

The asymmetry factor g can also be defined as the scattering diagram of the particle, which represents the angular distribution of the scattered radiation about a specified direction. If the particle scatters radiation isotropically, g is zero. If the particle scatters radiation in the forward direction, $g > 0$. If most of the radiation is scattered backward, $g < 0$.

The calculated asymmetry factors (g), the radiation pressure cross sections (C_{pr}), and the radiation pressure forces (F_{pr}) for silica microparticles (SiO_2, 1.00 and 2.50 μm in diameter), polystyrene microparticles (1.00, 2.00, and 3.00 μm in diameter), and macrophages are summarized in Table 1.

Separation of Microparticles Using FT-OC. To assess the capacity of FT-OC, separations of a mixture of two different sizes of SiO_2 microparticles and a mixture of three different sizes of PS microparticles were performed with a fixed laser power of 3 W. SiO_2 microparticles have a lower refractive index (~1.450)[19] than that of PS microparticles (~1.572).[20] At a total flow rate of 1400 nL/min, the average velocities determined for SiO_2 microparticles were 877.1 ± 16.4 μm/s for 1.00 μm SiO_2 microparticles (n = 771) and 673.5 ± 32.4 μm/s for 2.50 μm particles (n = 487). A baseline separation of two populations of SiO_2 microparticles based on their sizes was achieved, and the histogram is presented in Figure 1a. A higher total flow rate of 3000 nL/min was applied during the separation of PS particles (Figure 1b), and the measured average velocities were 1180.2 ± 18.9, 679.2 ± 13.4, and 342.4 ± 14.0 μm/s for 1.00 μm (n = 1213), 2.00 μm (n = 363), and 3.00 μm (n = 250) PS particles, respectively. It is worth mentioning that there were occasions in which more than one particle appeared in the detection window. Obviously, the optical forces exerted on a trailing particle were not the same as those on particles without a preceding particle. A filter for the "followers" in the software was used to remove these particles from the data set.

The force interactions on each single particle can be illustrated by following the trajectories of three differently sized PS microparticles. Figure 1c depicts the change in velocity of PS microparticles versus the x position as they were passing through the detection window carried by a fluid flow. At x position > 400 μm outside the focal region of the laser beam, all three differently sized particles had similar velocities. As the particles entered the focal region of the laser beam, the radiation pressure force, F_{pr}, caused deceleration of the particles at x < 300 μm, with larger particles displaying a greater decrease in velocities. After a short time (x < 200 μm), an equilibrium was reached where $F_{pr} = F_{drag}$ (F_{drag} is the drag force from the fluid flow), and the net force exerted on the particle became zero. The average velocities were determined within this region (x < 200 μm) for SiO_2 and PS microparticles are summarized in Table 1.

Comparisons were made between experimentally determined average velocities of particles (V_{exp}) and the calculated

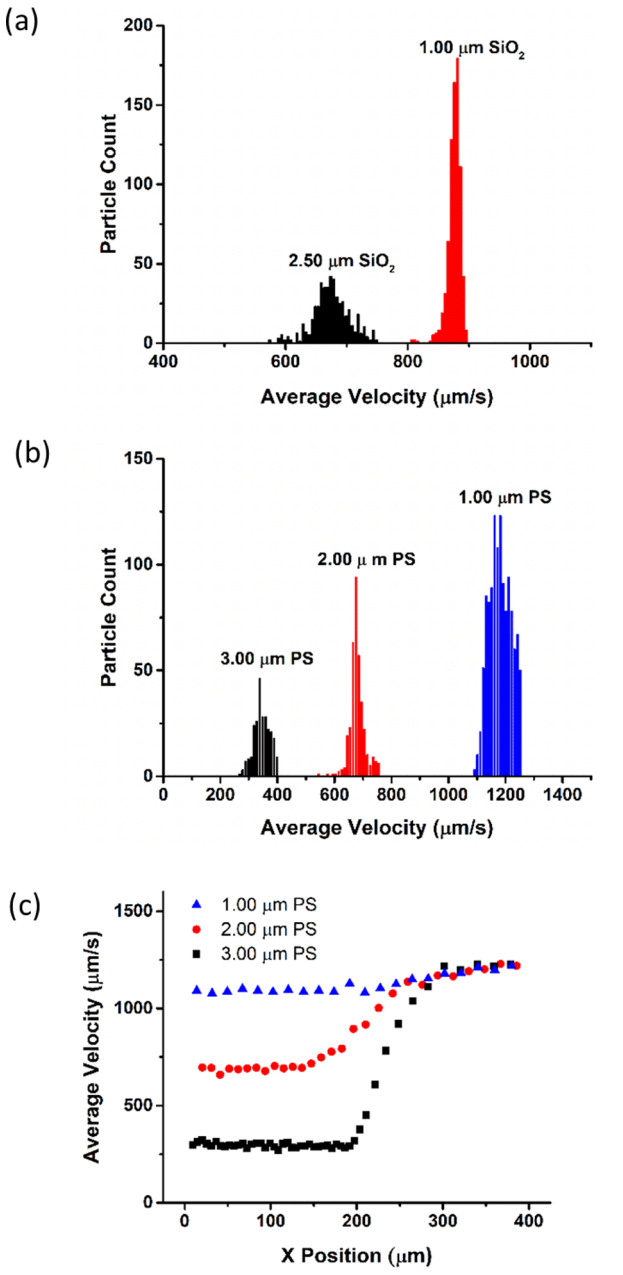

Figure 1. FT-OC separation of microparticles. Histogram of average velocities of (a) 1.00 and 2.50 μm SiO_2 and (b) 1.00, 2.00, and 3.00 μm PS microparticles. (c) Plots of the average velocity against the position of PS microparticles in parallel with the detection window.

velocities (V_{cal}), which were obtained using the radiation pressure force F_{pr} from Mie theory and the equilibrium condition $F_{pr} = F_{drag}$. If the particle is nearly spherical and suspended in a viscous and incompressible fluid with very small Reynolds numbers, F_{drag} is defined by Stokes' law[21]

$$F_{drag} = 6\pi\eta a V \tag{8}$$

where η denotes the dynamic viscosity, a is the radius of the spherical object, and V is the velocity of the particle relative to the fluid flow, which can be expressed as

$$V = V_{(laser-off)} - V_{cal} \tag{9}$$

where $V_{(laser-off)}$ is the velocity of the particle determined while the laser is turned off.

DOI: 10.1021/acsomega.9b01162
ACS Omega 2019, 4, 12938−12947

Applying the equilibrium condition

$$F_{pr} = F_{drag} = 6\pi\eta a(V_{(laser-off)} - V_{cal}) \quad (10)$$

V_{cal} values can be obtained, and they are in good agreement with V_{exp} values, thereby validating the setup for data collection and the data analysis of FT-OC.

Detection of the Responses of Macrophage Cells to Environmental Stimuli. *FT-OC.* Macrophages (200,000 cells/mL) were injected into the sample channel, and FT-OC was performed. With control cells freshly suspended in PBS (phosphate buffered saline, pH 7.4) and the total flow rate set at 2000 nL/min, the average size (the cross-sectional area of the cell) of this population was recorded as 79.6 ± 8.8 μm^2, which corresponds to an average cell diameter of 10.0 ± 1.1 μm. The average velocity was determined as 636.8 ± 36.0 μm/s (935 cells), which is in good agreement with the calculated velocity from the radiation pressure force F_{pr} obtained from Mie theory using a refractive index of 1.384,[22] the equilibrium condition $F_{pr} = F_{drag}$, and a cell diameter of 10.0 μm (see Table 1). Macrophages were next suspended in PBS for 2 h (subjected to nutritional deprivation) and analyzed by FT-OC. The average velocity for the population was determined as 590.0 ± 47.8 μm/s (767 cells), which is significantly slower than that for the macrophages not subjected to nutritional deprivation. The average diameter of the stressed macrophages increased slightly to 10.2 ± 1.3 μm, a small but statistically significant increase ($p < 0.001$) when compared to the control cells. The results of FT-OC from the control-cell population and the nutrient-deprived-cell population are presented in Figure 2a,b. FT-OC sensitively detected the changes in cell size and average velocity, but the slight increase in size for the nutrient-deprived cells (10.2 μm vs 10.0 μm) cannot be entirely responsible for the larger decrease in the average velocity (590.0 μm/s vs 636.8 μm/s). This discrepancy was further confirmed by the small differences in F_{pr} values (31.9 pN vs 30.5 pN) from Mie calculations solely based on the small size change and the resulting V_{cal} values (848.0 μm/s vs 876.0 μm/s) between the nutrient-deprived-cell population and the control-cell population. Further studies are necessary to identify the other contributing factors for the increase in radiation pressure force experienced by the stressed cell population. Note also that the piconewton-level laser forces experienced by the cells over subsecond timeframes are unlikely to impact cellular activity and viability.

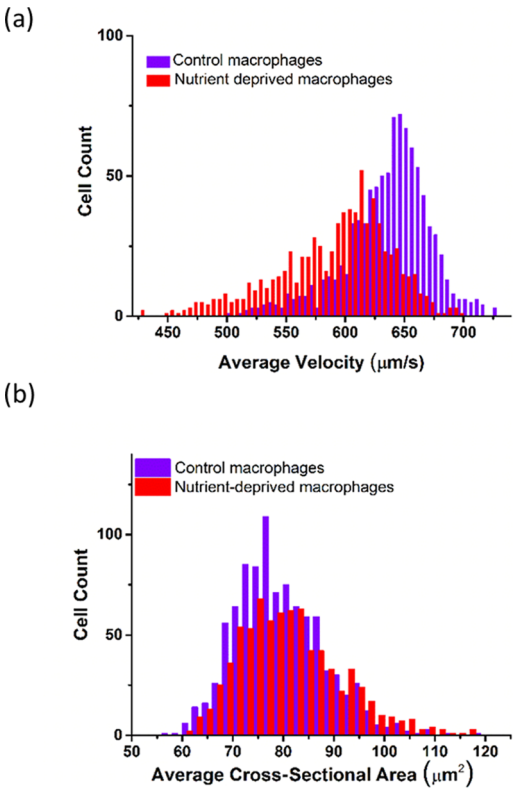

Figure 2. FT-OC separation of nutrient-deprived macrophages from control macrophages in (a) average velocity and (b) average cross-sectional area.

As shown in the radiation theory section, optical force and scattering are interrelated. Previous work on *Bacillus anthracis* spore uptake in macrophage cells showed qualitatively that 1064 nm radiation pressure differences experienced by cells before and after spore uptake were accompanied by significant side-scatter changes.[16] Thus, the optical force discrimination in this work indicates that changes in scattering may also occur for macrophages undergoing autophagy. Scatter measurements at 1064 nm, generally not used with commercial flow cytometers, may also offer improved discrimination in certain cases versus wavelengths in the visible region.[16] The refractive index and scattering are both wavelength-dependent, and higher power can be used at 1064 nm since biological samples are typically nonabsorbing in this region. Acquisition of quantitative scattering data in the OC configuration used for this work should also complement the force and imaging cytometry. This will be addressed in future work.

Nutritional deprivation can cause cell stress and is a well-known environmental stimulus that induces autophagy. It is likely that the difference detected in FT-OC between control and stressed cells reflects the changes resulting from cells undergoing autophagy. Various groups have experimentally determined that the actin cytoskeleton is involved in every stage of autophagy.[23−25] Actin-dependent cellular processes are typically associated with membrane dynamics, and the coordinated polymerization of actin filaments against cellular membranes provides the force for these processes.[26] It is not surprising that, due to the interplay between the actin cytoskeleton and the plasma membrane, remodeling of the cell membrane is also involved in autophagy. Reorganization of the actin cytoskeleton and remodeling of the plasma membrane induces morphological changes and may increase the F_{pr} experienced by nutrient-deprived cells. To validate the changes in the actin cytoskeleton and plasma membrane of stressed cells, differential interference contrast (DIC) microscopy, confocal fluorescence microscopy, and atomic force microscopy (AFM) were used to study fixed and stained cells as well as the live cells.

Optical Microscopy. To acquire higher resolution images of cells in suspension, that is, mimic the condition under which FT-OC was carried out, control and nutrient-deprived cells were fixed while they were in suspension, and their DIC images (Figure 3a) were obtained after cells settled at the bottom of a FluoroDish (World Precision Instruments, Sarasota, FL). The images of nutrient-deprived cells reveal substantial formation of filopodia. DIC and corresponding confocal fluorescence images of fixed, attached macrophages (both control and nutrient-deprived) further disclosed the distinct morphological differences between the two populations: the substantial formation of filopodia at the expense of lamellipodia and an

DOI: 10.1021/acsomega.9b01162
ACS Omega 2019, 4, 12938−12947

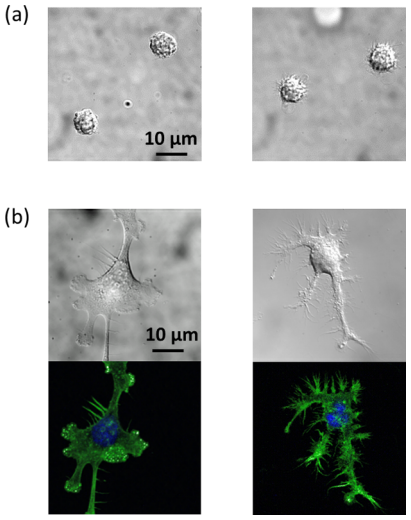

Figure 3. (a) DIC Images of fixed, suspended cells: control (left) and nutrient-deprived (right). (b) DIC and corresponding confocal fluorescence microscopy images (green: actin filament stain, blue: DAPI nuclear stain) of fixed attached cells: control (left) and nutrient-deprived (right).

overall decrease of podosomes in nutrient-deprived cells (Figure 3b). It is well known that lamellipodia are designed for persistent protrusion over a surface, and filopodia perform sensory and exploratory functions to steer cells depending on cues from the environment.[27] Arp2/3 complexes (actin-related protein 2/3) and formins are the two members of numerous different actin regulators that form the "right structure at the right place and time" within the cell.[28] Arp2/3 complexes promote the formation of lamellipod extensions.[29] Formins, on the other hand, are responsible for the formation of filopods.[30,31] Both Arp2/3 complexes and formins are important actin assembly factors in autophagy.[32] A competition between different assembly factors for finite monomeric actin to form different actin structures is a general mechanism at work within the actin cytoskeleton.[28] While macrophages respond to environmental stimuli, nutritional deprivation in this case, the substantial formation of filopodia structures was favored in accordance to their sensory and exploratory functions. The observed decrease in podosome structures in nutrient-deprived cells is probably related to the reduction of lamellipodia formation.

Atomic Force Microscopy. AFM images of live control and stressed cells were obtained using the QI mode with a set point of 400 pN. One of the major advantages of QI is the absence of lateral forces on live cells. A complete force−distance curve is recorded at each pixel, which can be used to determine Young's modulus values by fitting a Hertz model using JPK data processing software. Height images and pixel difference images are presented in Figure 4. As observed from our confocal microscopic studies, the nutrient-deprived cells exhibited more extensive filopodia formation with areas of rougher cell surfaces adjacent to these structures. Average Young's modulus values of the control cells (n = 5) were measured using an area of 1.5 × 1.5 μm at different locations that ranged from 6.10 ± 1.78 kPa at the cell height of 4.27 ± 0.07 μm on top of the nucleus to 17.66 ± 4.09 kPa at the cell height of 1.91 ± 0.12 μm near the outer edge. Corresponding values for nutrient-deprived cells (n = 5) were 5.97 ± 0.86 and 8.69 ± 0.75 kPa at cell heights of 5.64 ± 0.03 and 1.78 ± 0.10

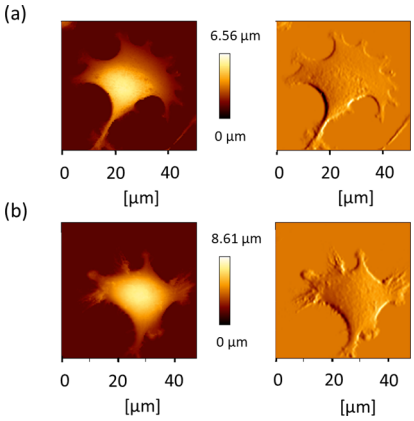

Figure 4. AFM height images (left) and pixel difference images (right) of (a) a control macrophage and (b) a nutrient-deprived macrophage.

μm, respectively. Generally, Young's modulus values are higher at the outer edges of the cells, and in these areas, stressed cells were softer than control cells. It is worth mentioning that during data acquisition using the QI mode on live cells, the indentation depth never exceeded 500 nm; therefore, the impact from the substrate underneath the cells should be negligible.

Confocal Raman Microspectroscopy. DIC images, confocal fluorescence images, AFM images, and Young's modulus values confirmed the changes in morphology and membrane elasticity of stressed cells induced by nutritional deprivation. Confocal Raman microspectroscopy is an additional method that is sensitive to biochemical changes reflecting physiological states and processes in cells.[33] In this work, we utilized resonance Raman sensitivity to cytochrome Fe(II)/Fe(III) redox states[34,35] as an indicator of cellular response to nutritional deprivation. At 514 nm, excitation signal enhancements from macrophages were detected at 1584, 1397, 1362, 1312, and 1172 cm^{-1}, attributed primarily to reduced cytochrome c (Figure 5d).[35] This particular signal enhancement will decrease when cytochrome redox ratios shift to greater oxidized levels, and the sensitivity is found to provide a particularly strong biomarker of the cellular response to PBS versus media. To compare cells, the 1172 cm^{-1} peak area was normalized against the 1003 cm^{-1} phenylalanine peak area (generally a representative signal for proteins). Both of these peaks are in regions that showed little interference from other Raman bands. Figure 5a,b presents a comparison of Raman maps of the 1172/1003 cm^{-1} ratios for four cells in media and four cells at 2−3 h after transferring from media to PBS. These images show that 1172 cm^{-1} relative intensities are consistently low for nutrient-deprived cells (all maps are shown on the same relative scale). This is further quantified in Figure 5e, which shows histograms of the composite top 10 intensity values from each of the four images in Figure 5a,b. The clear demarcation demonstrates confocal Raman microspectroscopy as a valuable complimentary method in combination with FT-OC for cell analysis.

Figure 5c further demonstrates the sensitivity to time-dependent changes on a single cell in PBS. The left image shows the 1172/1003 cm^{-1} map at an early time point (approximately 1 h) after transfer to PBS, and the right image shows the same cell approximately 2 h later. The later time-point image also shows the characteristic "darkening"

DOI: 10.1021/acsomega.9b01162
ACS Omega 2019, 4, 12938−12947

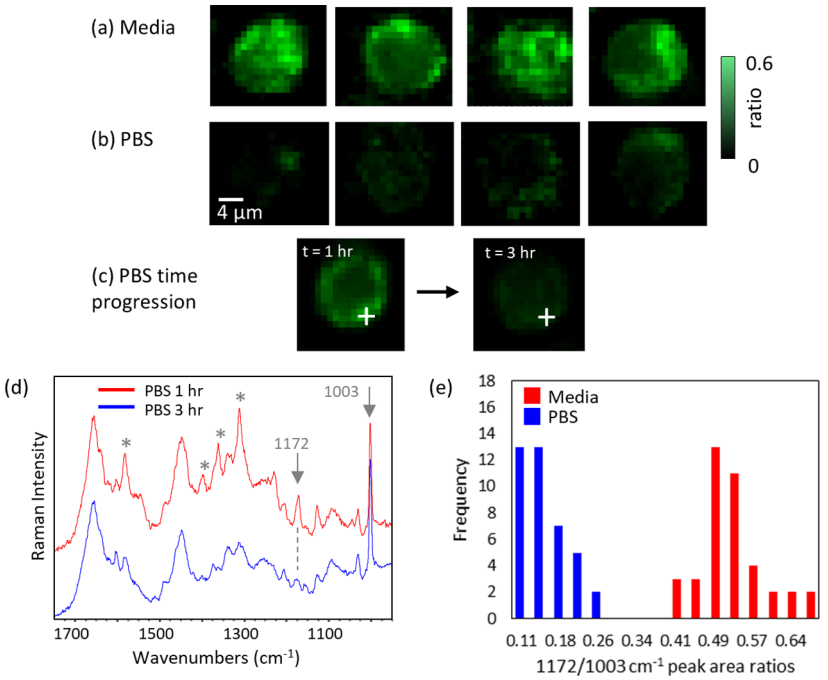

Figure 5. Raman maps of the 1172/1003 cm^{-1} peak area ratios for individual cells in (a) media and (b) PBS. All images are scaled relative to the 4 μm scale bar. (c) Raman maps of the 1172/1003 cm^{-1} peak area ratios for a macrophage cell in PBS for 1 h (left) and the same cell after 3 h in PBS (right). (d) Spectra acquired at the "+" annotations in the time-dependent PBS images. The 1172 and 1003 cm^{-1} peaks used to generate the maps are identified at the arrows, and the "*" annotations identify the additional 1584, 1397, 1362, and 1312 cm^{-1} peaks that are also associated with reduced state cytochrome resonance enhancement. (e) Histograms of the composite top 10 intensity values from each of the four images in (a) and (b).

corresponding to shifting of the cytochrome redox ratios to greater oxidized levels. Examples of spectra acquired at similar locations (the "+" annotations) at the different time points in Figure 5c are given in Figure 5d. The 1172 and 1003 cm^{-1} cytochrome and phenylalanine peaks used to generate the normalized Raman maps are identified along with additional cytochrome-related peaks that indicate resonance enhancement at the 1 h time point.

Cytochromes are involved in many redox biochemistry processes, but their primary function is in electron transport chains for mitochondrial respiration.[36] They are additionally associated with generation of reactive oxygen species, which can play roles in signaling mechanisms, but imbalances can lead to oxidative stress as well. These factors have also been associated with the onset of autophagy.[37] In our case, the lack of oxidizable substrates under nutritional deprivation conditions is regarded as the primary mechanism leading to the observed shift in cytochrome redox ratios. Mitochondrial electron leakage will further drive the ratios to greater oxidation.[37]

A Raman biomarker for autophagy associated with a phospholipid increase has also been previously demonstrated for mouse and human cancer cells under nutritional deprivation over periods of 2−5 days.[38] This was thought to be related to the increased level of vesicle walls from generation of autophagosomes. We did not detect a significant difference in phospholipid-related peaks in our data, but this is probably a result of the much shorter starvation timescales. Rather, the strong differentiation of cytochrome redox ratios can be signified as a potentially early and predictive indicator of the onset of autophagy.

CONCLUSIONS

The capacity of a higher-throughput label-free FT-OC technology utilizing the counteraction of a radiation pressure force, F_{pr}, and a drag force, F_{drag}, was demonstrated by the rapid baseline separation of a mixture of SiO_2 microparticles and a mixture of PS microparticles based on size differences. Experimentally determined average velocities of the microparticles agreed with the calculated values using F_{pr} from the Mie scattering equation and F_{drag} from the Stokes equation at equilibrium. The sensitivity of FT-OC enabled the detection of the responses of macrophage cells to environmental stimuli, such as nutritional deprivation, as a decrease in the average velocity accompanied by a small increase in the average cell size. Other changes revealed by confocal fluorescence microscopy, AFM, and confocal Raman microspectroscopy include cell morphological changes induced by reorganization of the actin cytoskeleton and remodeling of the plasma membrane as well as biochemical transformations of the cells manifested by alterations in cytochrome redox states. The reorganization of the cytoskeleton changed the distribution of the actin structure and altered the scattering pattern. The remodeling of the plasma membrane displayed ruffled characteristics that increased light scattering. The combination of all these factors contributed to the increase in radiation pressure force exerted on the nutrient-deprived cells, which resulted in their average velocity being reduced. This work has demonstrated that label-free, high-throughput FT-OC, in combination with confocal Raman microspectroscopy, holds the potential to become a timely pathogen detection method based on changes in the radiation pressure force experienced by innate immune cells. The innate immune cells, such as macrophages, thus serve as a proxy for detecting host immune

DOI: 10.1021/acsomega.9b01162
ACS Omega 2019, 4, 12938−12947

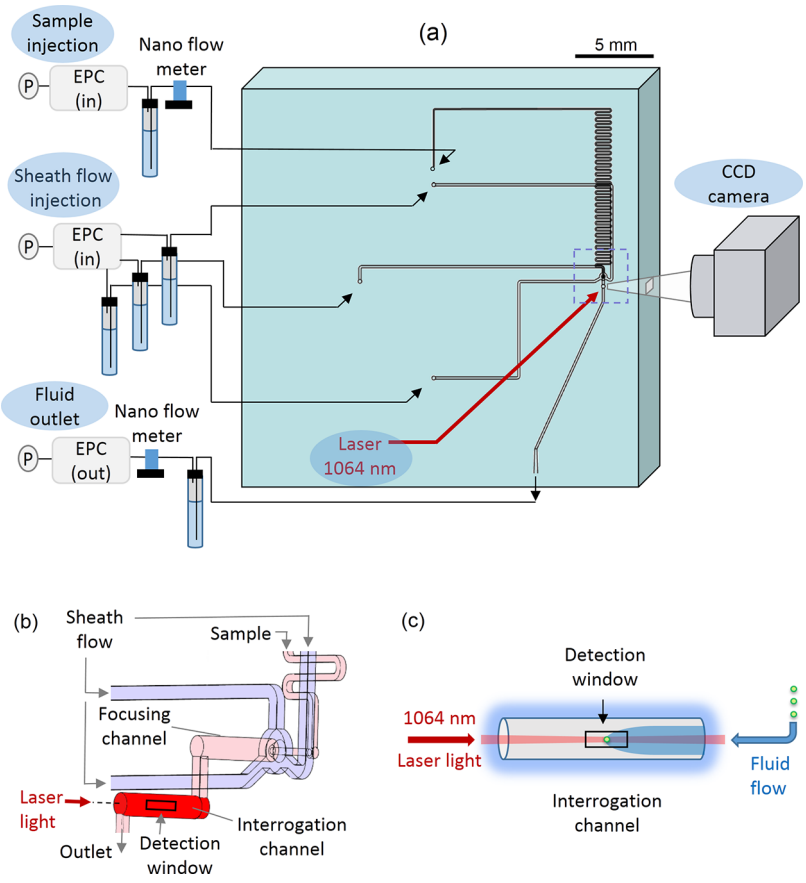

Figure 6. (a) Schematic of the FT-OC system. (b) 3D focusing nozzle leading to the focusing channel and interrogation channel. (c) Working principle of FT-OC: balancing optical force and drag force on a microparticle.

responses via associated physical and biochemical cellular changes.

MATERIALS AND METHODS

Cell Culture. Mouse peritoneal macrophage cells (IC-21) were obtained from ATCC (Manassas, VA, USA) and grown at 37 °C in the presence of 5% CO_2 in RPMI-1640 media supplemented with 10% fetal calf serum (ATCC). The cells were seeded 24−48 h prior to performing the assays.

FT-OC System Setup. A schematic of the FT-OC system is given in Figure 6a. The microfluidic flow cell was custom-fabricated by Translume Inc. (Ann Arbor MI) and consisted of five layers of fused silica plates. The side lengths of the plates are 25.4 mm with a thickness varying from 0.5 to 1 mm. Three holes 350 μm in diameter were drilled in one of the two cover plates to connect the liquid reservoirs to three sheath flow channels leading to a 3D focusing nozzle (Figure 6b) constructed at the beginning of a circular focusing channel (250 μm in diameter). One hole, 350 μm in diameter, was drilled in the other cover plate to connect the sample reservoir to the sample injection channel leading toward the center of the focusing nozzle. A serpentine channel was incorporated in the sample injection channel to entrain injected particles/cells at low flow rates. The second circular channel (250 μm in diameter) downstream of the focusing channel served as the interrogation region for particles/cells (Figure 6b). A custom-made plastic flow cell holder was used to create leak-free connections between the channel inlets/outlets and fluid connectors (Nanoport, Upchurch Scientific, Inc., Oak Harbor, WA).

The fluid control system consisted of five pressurized fluid reservoirs using PEEK capillaries (100 μm in inner diameter, IDEX, Lake Forest, Illinois, U.S.A.) and fluid connectors from IDEX. Three fluid reservoirs were used for three sheath flows, and one was used for sample injection. The fifth reservoir was connected to the outlet of the flow cell. Pulseless, stable, and reproducible fluid flows were enabled by electronic pressure controllers (OEM-EP, Parker Hannifin, Hollis, NH). Flow directions and flow rates were controlled by in-house software developed using LabView. Flow rates were measured to a resolution of 1.5 nL/min using multiple calibrated liquid mass flow meters (Sensirion Inc., Palo Alto, CA).

Optics and Imaging. A continuous-wave (CW) 1064 nm ytterbium fiber laser (IPG Photonics, Oxford, MA) was used to impart an optical force on the particles/cells to be analyzed. The laser beam was focused into the interrogation channel by a 0.5 inch-in-diameter, 75 mm-in-focal length lens from Thorlabs (Newton, NJ). The focusing and interrogation channels were monitored using either a 10× or a 20× objective (Mitutoyo, Kawasaki, Japan) and a lens tube system (Infinity Photo-Optical, Boulder, CO) connected to a CCD camera (Basler, Inc. Exton, PA) illuminated using a PL-800 fiber optic light (Edmund Optics, Barrinton, NJ). The camera, objective, and illuminator were mounted independent of the laser and of each other on separate *xyz* translation platforms from Thorlabs. The alignment of the laser beam inside the interrogation channel was achieved by imaging injected fluorescent polystyrene

DOI: 10.1021/acsomega.9b01162
ACS Omega 2019, 4, 12938−12947

microspheres (Fluoresbrile carboxy YO 0.2 micron, Polysciences, Warrington, PA) that filled the channel. Beam waist (19.8 μm) was measured after the alignment.

FT-OC Data Collection and Analysis. Particles used were SiO_2 (1.00 and 2.50 μm in diameter, Polysciences, Warrington, PA) and PS (1.00, 2.00, and 3.00 μm in diameter, Polysciences) suspended in DI H_2O in appropriate concentrations. Live macrophage samples were prepared as described below. The seeded cells were first rinsed with room temperature PBS (1×) twice (Life Technologies, Carlsbad, CA) and then were dislodged from the 6-well plate (USA Scientific, Ocala, FL) by incubating the plate at 37 °C with 2 mL of PBS (1×) for 5−7 min. The cells were collected and centrifuged at 125 × g for 5 min. The supernatant was discarded, and the pellet was resuspended in 1 mL of PBS (1×), and the cell density was determined using a hemocytometer. A cell density of 200,000 cells in 1 mL of PBS (1×) was used for the assay. For the nutrient-deprived cells, the cells were processed similarly and were subsequently suspended in PBS for 2 h prior to FT-OC data collection.

FT-OC was performed by applying two opposing forces on particles/cells using a laser beam (radiation pressure force, F_{pr}) and a fluid flow (drag force, F_{drag}), as shown in Figure 6c. At a fixed laser power, usually 3 W, an appropriate total fluid flow rate (the sum of three sheath flows and the sample injection flow) was chosen to ensure that the particles/cells passing through the interrogation window were not stopped by the optical force. Particles/cells were continuously injected into the sample channel from the sample reservoir with a flow rate approximately 10% of the total flow rate. The sample stream met the three sheath flows at the 3D focusing nozzle with particles/cells confined to the center core of the flow toward the interrogation channel. Data collection and analysis were performed using in-house software. Briefly, a detection window (400 × 125 μm) was centered at the focal region of the laser beam as indicated by the black box in Figure 6c. As each particle enters the detection window, its images were recorded by the CCD camera (50 fps), and the x positions (parallel to the flow direction) of these images were determined by the software. The average particle velocity was calculated from recorded images and their positions. The average particle size was determined by counting the number of pixels in the images. Each day before running actual samples, the laser alignment and the beam focal point were calibrated by collecting a number of 3 μm PS particles (n > 100) under preset conditions. Necessary adjustments were made to ensure the reproducibility of the average velocities and the positions of the particles along the detection window at their slowest velocities under the same preset conditions.

DIC and Confocal Fluorescence Microscopy Studies of Macrophages. For DIC imaging of fixed suspended cells, the cells were rinsed twice with PBS (1×), and fresh PBS was added to the cells, and they were allowed to incubate for 5−7 mins to dislodge the attached the cells. The dislodged cells were collected and centrifuged at 125g for 5 mins. The supernatant was discarded, and the cell pellet was resuspended in 1 mL of PBS. An equal volume (1 mL) of 4% paraformaldehyde (Sigma-Aldrich, St. Louis, MO) was added to the cells. The cells were incubated for 10 mins at room temperature and then were centrifuged at 125g for 5 mins. The supernatant was discarded, and the fixed cell pellet was resuspended in 1 mL of PBS before analysis. The same protocol was followed for nutrient-deprived cells except dislodged cells were kept in suspension in PBS for 2 h on the working bench at room temperature prior to the fixation. The procedure of preparing samples for DIC and confocal fluorescence imaging of fixed attached cells are described below. Approximately 1500 cells were seeded in the center of a FluoroDish in culture media and incubated at 37 °C in the presence of 5% CO_2 for 24 h prior to performing the confocal staining. After 24 h, the cells were washed twice with PBS (1×) and 2% glutaraldehyde (Sigma-Aldrich, St. Louis, MO) was added to the cells followed by 45 s incubation at 37 °C under 5% CO_2. The cells were then rinsed twice with PBS (1×), and 4% paraformaldehyde was added to the cells. After 20 min of incubation at room temperature, the cells were washed twice with PBS (1×) before adding 1% Triton-X-100 (Sigma-Aldrich, St. Louis, MO). After 5 min, the cells were washed again, twice with PBS (1×). For blocking, 1% BSA (ThermoFisher Scientific, Pittsburgh, PA) was added to the cells, and the sample was incubated at RT for 30 min before washing twice with PBS (1×). The actin filament stain, Alex Fluor 488 Phalloidin stain (1:500) (Ex/Em: 495/518 nm, Life Technologies, Carlsbad, CA), was added to the cells, and the cells were incubated in the dark for 20 min. The cells were washed twice with PBS (1×) and a drop of the DAPI nuclear stain (Ex/Em: 360/460 nm, Vector Laboratories, Burlingame, CA) was added onto the cells. The same protocol was followed for nutrient-deprived cells except the cells were incubated in PBS for 30 min prior to the fixation.

DIC images were acquired on a Nikon Eclipse Ti inverted confocal microscope with a 100× oil objective lens (NA 1.49, Nikon). A 405 nm OBIS laser and a 488 nm Sapphire laser (both from Coherent, Santa Clara, CA) were used to acquire confocal fluorescence images.

AFM of Live Macrophages. Cells with a density of 750 cells/mL were seeded at the center of a FluoroDish coated with poly-D-lysine 24 h prior to AFM measurement. For cells used in the nutritional deprivation study, the culture medium in the FluoroDish was replaced with PBS 30 min prior to AFM scanning. AFM images were obtained using a NanoWizard 4a AFM (JPK Instruments AG, Berlin, Germany) mounted on an Eclipse Ti-E inverted microscope (Nikon Instruments Inc. Melville, NY). AFM scans are performed in the QI mode at room temperature using qp-BioAC-CB3 AFM probes (NANOSENSORS, CH-2000 Neuchatel, Switzerland).

Confocal Raman Microspectroscopy of Macrophages. The cells were processed using the same procedure as mentioned for OC. Cells suspended in cell culture media or PBS in a screw cap tube (1 mL, 100,000 cells/mL) were poured into a petri dish filled with 3 mL of the medium or PBS. Cells were allowed to settle onto a glass coverslip at the bottom of the dish before a water dipping objective (100×/NA 1.10, Nikon) was immersed. Confocal Raman spectra of cells were acquired while they were still in a spherical morphology with a Renishaw inVia Raman upright microscope (Gloucestershire, United Kingdom) using a 514 nm argon laser with 2400 lines/mm grating. Spectra were acquired from 530 to 1800 cm^{-1}, and mapping step sizes were 1 μm in the x and y directions. Raman data was processed and analyzed using WIRE 4.1 software (Renishaw). Processing consisted of cosmic ray spike removal and principal component noise filtering. Maps were then generated from selected Raman peak areas. No corrections were made for cells either in media or PBS. Using a confocal configuration and a high NA objective minimized background contributions from media/PBS.

DOI: 10.1021/acsomega.9b01162
ACS Omega 2019, 4, 12938−12947

Radiation Pressure Calculation Using Mie Theory. Calculations were performed utilizing a modified code from Dave[39] to obtain the asymmetry parameter g for spherical polystyrene, silica particles, and macrophage cells. The asymmetry parameter is the average cosine of the laser light scattering angle. The particles were assumed to have a real refractive index ($Q_{abs} = 0$). The extinction efficiencies from the Dave code were compared with the results from the Bohren–Huffman code[40] and were in good agreement. The particles were suspended in water ($n = 1.326$). The laser wavelength was 1064 nm, and the power was 3.0 W.

AUTHOR INFORMATION

Corresponding Author

*E-mail: qin.lu@nrl.navy.mil.

ORCID

Qin Lu: 0000-0002-5205-1112

Daniel E. Barlow: 0000-0002-8009-5710

Present Addresses

†J.D.G.: The Geneva Foundation, 917 Pacific Avenue, Tacoma, Washington 98402, United States

‡A.V.T.: MRIGlobal, 65 W Watkins Mill Road, Gaithersburg, Maryland 20878, United States

Notes

The authors declare no competing financial interest.

ACKNOWLEDGMENTS

The authors would like to acknowledge the Office of Naval Research and the Naval Research Laboratory for funding this research.

REFERENCES

(1) Adan, A.; Alizada, G.; Kiraz, Y.; Baran, Y.; Nalbant, A. Flow cytometry: basic principles and applications. *Crit. Rev. Biotechnol.* **2015**, *37*, 163–176.

(2) Cheung, K. C.; Di Berardino, M.; Schade-Kampmann, G.; Hebeisen, M.; Pierzchalski, A.; Bocsi, J.; Mittag, A.; Tárnok, A. Microfluidic impedance-based flow cytometry. *Cytometry, Part A* **2010**, *77A*, 648–666.

(3) Otto, O.; Rosendahl, P.; Mietke, A.; Golfier, S.; Herold, C.; Klaue, D.; Girardo, S.; Pagliara, S.; Ekpenyong, A.; Jacobi, A.; Wobus, M.; Töpfner, N.; Keyser, U. F.; Mansfeld, J.; Fischer-Friedrich, E.; Guck, J. Real-time deformability cytometry: on-the-fly cell mechanical phenotyping. *Nat. Methods* **2015**, *12*, 199.

(4) Stavrakis, S.; Holzner, G.; Choo, J.; deMello, A. High-throughput microfluidic imaging flow cytometry. *Curr. Opin. Biotechnol.* **2019**, *55*, 36–43.

(5) Dochow, S.; Krafft, C.; Neugebauer, U.; Bocklitz, T.; Henkel, T.; Mayer, G.; Albert, J.; Popp, J. Tumour cell identification by means of Raman spectroscopy in combination with optical traps and microfluidic environments. *Lab Chip* **2011**, *11*, 1484–1490.

(6) Hiramatsu, K.; Ideguchi, T.; Yonamine, Y.; Lee, S.; Luo, Y.; Hashimoto, K.; Ito, T.; Hase, M.; Park, J.-W.; Kasai, Y.; Sakuma, S.; Hayakawa, T.; Arai, F.; Hoshino, Y.; Goda, K. High-throughput label-free molecular fingerprinting flow cytometry. *Sci. Adv.* **2019**, *5*, No. eaau0241.

(7) Kaneta, T.; Ishidzu, Y.; Mishima, N.; Imasaka, T. Theory of Optical Chromatography. *Anal. Chem.* **1997**, *69*, 2701–2710.

(8) Hart, S. J.; Terray, A.; Leski, T. A.; Arnold, J.; Stroud, R. Discovery of a Significant Optical Chromatographic Difference between Spores of Bacillus anthracis and Its Close Relative. *Anal. Chem.* **2006**, *78*, 3221–3225.

(9) Hebert, C. G.; Terray, A.; Hart, S. J. Toward Label-Free Optical Fractionation of Blood—Optical Force Measurements of Blood Cells. *Anal. Chem.* **2011**, *83*, 5666–5672.

(10) Ashkin, A. Acceleration and Trapping of Particles by Radiation Pressure. *Phys. Rev. Lett.* **1970**, *24*, 156–159.

(11) Grier, D. G. A revolution in optical manipulation. *Nature* **2003**, *424*, 810–816.

(12) Taylor, J. D.; Terray, A.; Hart, S. J. Analytical particle measurements in an optical microflume. *Anal. Chim. Acta* **2010**, *670*, 78–83.

(13) Kim, S. Y.; Taylor, J. D.; Ladouceur, H. D.; Hart, S. J.; Terray, A. Radiation pressure efficiency measurements of nanoparticle coated microspheres. *Appl. Phys. Lett.* **2013**, *103*, 234101.

(14) Klionsky, D. J.; Baehrecke, E. H.; Brumell, J. H.; Chu, C. T.; Codogno, P.; Cuervo, A. M.; Debnath, J.; Deretic, V.; Elazar, Z.; Eskelinen, E.-L.; Finkbeiner, S.; Fueyo-Margareto, J.; Gewirtz, D. A.; Jäättelä, M.; Kroemer, G.; Levine, B.; Melia, T. J.; Mizushima, N.; Rubinsztein, D. C.; Simonsen, A.; Thorburn, A.; Thumm, M.; Tooze, S. A. A comprehensive glossary of autophagy-related molecules and processes (2nd edition). *Autophagy* **2011**, *7*, 1273–1294.

(15) Vural, A.; Kehrl, J. H. Autophagy in Macrophages: Impacting Inflammation and Bacterial Infection. *Scientifica* **2014**, *2014*, 825463.

(16) Hebert, C. G.; Hart, S.; Leski, T. A.; Terray, A.; Lu, Q. Label-Free Detection of *Bacillus anthracis* Spore Uptake in Macrophage Cells Using Analytical Optical Force Measurements. *Anal. Chem.* **2017**, *89*, 10296–10302.

(17) Kerker, M. *The scattering of light and other electromagnetic radiation: physical chemistry: a series of monographs*; Academic press: New York, London, 1969.

(18) *Fundamental Optics, The CVI Melles Griot Technical Guide*; CVI Melles Griot, 2009; Vol. *2*.

(19) Malitson, I. H. Interspecimen Comparison of the Refractive Index of Fused Silica. *J. Opt. Soc. Am.* **1965**, *55*, 1205–1209.

(20) Kasarova, S. N.; Sultanova, N. G.; Ivanov, C. D.; Nikolov, I. D. Analysis of the dispersion of optical plastic materials. *Opt. Mater.* **2007**, *29*, 1481–1490.

(21) Happel, J.; Brenner, H. *Low Reynolds number hydrodynamics*; Martinus Nijhoff Publishers: Hingham, MA, 1983.

(22) Neto, J. C.; Agero, U.; Gazzinelli, R. T.; Mesquita, O. N. Measuring optical and mechanical properties of a living cell with defocusing microscopy. *Biophys. J.* **2006**, *91*, 1108–1115.

(23) Aplin, A.; Jasionowski, T.; Tuttle, D. L.; Lenk, S. E.; Dunn, W. A., Jr. Cytoskeletal elements are required for the formation and maturation of autophagic vacuoles. *J. Cell. Physiol.* **1992**, *152*, 458–466.

(24) Aguilera, M. O.; Berón, W.; Colombo, M. I. The actin cytoskeleton participates in the early events of autophagosome formation upon starvation induced autophagy. *Autophagy* **2014**, *8*, 1590–1603.

(25) Zhuo, C.; Ji, Y.; Chen, Z.; Kitazato, K.; Xiang, Y.; Zhong, M.; Wang, Q.; Pei, Y.; Ju, H.; Wang, Y. Proteomics analysis of autophagy-deficient Atg7−/− MEFs reveals a close relationship between F-actin and autophagy. *Biochem. Biophys. Res. Commun.* **2013**, *437*, 482–488.

(26) Saarikangas, J.; Zhao, H.; Lappalainen, P. Regulation of the Actin Cytoskeleton-Plasma Membrane Interplay by Phosphoinositides. *Physiol. Rev.* **2010**, *90*, 259–289.

(27) Mejillano, M. R.; Kojima, S.-i.; Applewhite, D. A.; Gertler, F. B.; Svitkina, T. M.; Borisy, G. G. Lamellipodial versus filopodial mode of the actin nanomachinery: pivotal role of the filament barbed end. *Cell* **2004**, *118*, 363–373.

(28) Davidson, A. J.; Wood, W. Unravelling the Actin Cytoskeleton: A New Competitive Edge? *Trends Cell Biol.* **2016**, *26*, 569–576.

(29) Svitkina, T. M.; Borisy, G. G. Arp2/3 Complex and Actin Depolymerizing Factor/Cofilin in Dendritic Organization and Treadmilling of Actin Filament Array in Lamellipodia. *J. Cell Biol.* **1999**, *145*, 1009–1026.

(30) Schirenbeck, A.; Bretschneider, T.; Arasada, R.; Schleicher, M.; Faix, J. The Diaphanous-related formin dDia2 is required for the formation and maintenance of filopodia. *Nat. Cell Biol.* **2005**, *7*, 619.

(31) Pellegrin, S.; Mellor, H. The Rho Family GTPase Rif Induces Filopodia through mDia2. *Curr. Biol.* **2005**, *15*, 129–133.

DOI: 10.1021/acsomega.9b01162
ACS Omega 2019, 4, 12938–12947

(32) Kruppa, A. J.; Kendrick-Jones, J.; Buss, F. Myosins, Actin and Autophagy. *Traffic* **2016**, *17*, 878−890.
(33) Smith, R.; Wright, K. L.; Ashton, L. Raman spectroscopy: an evolving technique for live cell studies. *Analyst* **2016**, *141*, 3590−3600.
(34) Brazhe, N. A.; Treiman, M.; Brazhe, A. R.; Find, N. L.; Maksimov, G. V.; Sosnovtseva, O. V. Mapping of Redox State of Mitochondrial Cytochromes in Live Cardiomyocytes Using Raman Microspectroscopy. *PLoS One* **2012**, *7*, No. e41990.
(35) Kakita, M.; Kaliaperumal, V.; Hamaguchi, H.-o. Resonance Raman quantification of the redox state of cytochromes b and c in-vivo and in-vitro. *J. Biophotonics* **2012**, *5*, 20−24.
(36) Cooper, G. M.; Hausman, R. E. *The Cell, a molecular approach*; ASM Press: Washington, DC, 2009.
(37) Filomeni, G.; De Zio, D.; Cecconi, F. Oxidative stress and autophagy: the clash between damage and metabolic needs. *Cell Death Differ.* **2015**, *22*, 377.
(38) Konorov, S. O.; Jardon, M. A.; Piret, J. M.; Blades, M. W.; Turner, R. F. B. Raman microspectroscopy of live cells under autophagy-inducing conditions. *Analyst* **2012**, *137*, 4662−4668.
(39) Dave, J. V. Scattering of Electromagnetic Radiation by a Large, Absorbing Sphere. *IBM J. Res. Dev.* **1969**, *13*, 302−313.
(40) Bohren, C. F.; Huffman, D. R. *Absorption and Scattering of Light by Small Particles*; John Wiley and Sons: New York, 1983.

DOI: 10.1021/acsomega.9b01162
ACS Omega 2019, 4, 12938−12947